Title
A fundamental look at electrocatalytic sulfur reduction reaction

Journal
NATURE CATALYSIS, 3(9)

ISSN
2520-1158

Authors
Peng, Lele
Wei, Ziyang
Wan, Chengzhang
et al.

Publication Date
2020-09-01

DOI
10.1038/s41929-020-0498-x

Peer reviewed

A fundamental look at electrocatalytic sulfur reduction reaction

Lele Peng[1], Ziyang Wei[1], Chengzhang Wan[1], Jing Li[1], Zhuo Chen[2], Dan Zhu[1], Daniel Baumann[1], Haotian Liu[2], Christopher S. Allen[3,4], Xiang Xu[1], Angus I. Kirkland[3,4], Imran Shakir[2,5], Zeyad Ammar Almutairi[5], Sarah Tolbert[1,6], Bruce Dunn[2,6], Yu Huang[2,6*], Philippe Sautet[1,7*], Xiangfeng Duan[1,6*]

[1]*Department of Chemistry and Biochemistry, University of California, Los Angeles, CA 90095, USA.* [2]*Department of Materials Science and Engineering, University of California, Los Angeles, CA 90095, USA.* [3]*Departments of Materials, University of Oxford, Oxford OX1 2JD, UK.* [4]*Electron Physical Sciences Imaging Centre (ePSIC), Diamond Light Source, Didcot OX11 0DE, Oxford, UK.* [5]*Sustainable Energy Technologies Centre, College of Engineering, King Saud University, Riyadh 11421, Saudi Arabia.* [6]*California NanoSystems Institute, University of California, Los Angeles, CA 90095, USA.* [7]*Department of Chemical and Biomolecular Engineering, University of California, Los Angeles, CA 90095, USA.*

**To whom correspondence should be addressed.* xduan@chem.ucla.edu (X.D.); sautet@ucla.edu (P.S.); yhuang@seas.ucla.edu (Y.H.)

The fundamental kinetics of the electrocatalytic sulfur reduction reaction (SRR), a complex 16-electron conversion process in lithium-sulfur batteries, is insufficiently explored to date. Herein, by directly profiling the activation energies in the multi-step SRR, we reveal that the initial reduction of sulfur to the soluble polysulfides is relatively easy with low activation energy, while the subsequent conversion of the polysulfides into the insoluble Li_2S_2/Li_2S is more difficult with much higher activation energy, which contribute to the accumulation of polysulfides and exacerbate the polysulfide shuttling effect. We use heteroatom-doped graphene as a model system to explore electrocatalytic SRR. We show nitrogen and sulfur dual-doped graphene considerably reduces the activation energy to improve SRR kinetics. Density functional calculations confirm that the doping tunes the *p*-band center of the active carbons for an optimal adsorption strength of intermediates and electroactivity. This study establishes electrocatalysis as a promising pathway to high performance lithium-sulfur batteries.

The sulfur reduction reaction (SRR) in lithium-sulfur (Li-S) chemistry undergoes a complex 16-electron conversion process, transforming S_8 ring molecules into a series of soluble lithium polysulfides (LiPSs) with variable chain lengths before fully converting them into

insoluble Li_2S_2/Li_2S products. This 16-electron SRR process is of considerable interest for high-density energy storage with theoretical capacity of 1672 mAh g^{-1}, but the chemistry is plagued by sluggish sulfur reduction kinetics and polysulfide (PS) shuttling effect. In practical Li-S cells, these effects limit the rate capability and cycle life[1,2]. These limitations are fundamentally associated with the slow and complex reduction reaction involving S_8 ring molecules. In general, the insulating nature of elemental sulfur and its reduced products, and the sluggish charge transfer kinetics lead to incomplete conversion of S_8 molecules to soluble LiPSs. These polysulfides may shuttle across the separator to react with and deposit on the lithium anode, resulting in rapid capacity fading[3]. Considerable efforts have been devoted to combating the PS shuttling effect, typically by employing a passive strategy by using various sulfur host materials to physically or electrostatically trap the LiPSs in the cathode structure[4-13]. These passive confinement/entrapping strategies have partly mitigated the PS shuttling effect and led to improved performance, but are fundamentally incapable of completely preventing the dissolution of LiPSs into the electrolyte and eliminating the PS shuttling effect.

The PS shuttling effect originates from the formation, dissolution and accumulation of LiPS intermediates in the electrolyte. In this regard, the slow conversion kinetics of the soluble LiPSs into the insoluble final products leads to continued accumulation of LiPSs in electrolyte that exacerbates the PS shuttling effect[14-15]. To this end, an electrocatalytic approach to accelerate the conversion of soluble LiPS intermediates into insoluble Li_2S_2/Li_2S appears to be a natural strategy to prevent the accumulation and shuttling of LiPSs. In this way, the use of electrocatalysis would address the PS shuttling effect while at the same time improve the rate capability. Although the concept of an electrocatalytic approach has been suggested in a few recent studies[16-18], the fundamental electrocatalytic kinetics of SRR are largely unexplored and the underlying basis for using such an electrocatalytic effect to address the PS shuttling issues has not been considered.

Herein, we report a systematic investigation of electrocatalytic SRR kinetics. To understand the catalytic performance of various heteroatom-doped holey graphene framework (HGF) electrocatalysts and their impact on battery performance, we focus on fundamental electrocatalytic studies by systematically probing the reduction kinetics, the activation energies and the reduction mechanisms. By directly profiling the activation energies in the multi-step SRR, we establish how the conversion kinetics differ for each step, and reveal that the initial reduction of S_8 ring molecules to the soluble PSs is relatively easy with low activation energy,

while the subsequent conversion of the PSs into the insoluble Li_2S_2/Li_2S is more difficult with much higher activation energy. This slow polysulfide conversion kinetics contributes to the accumulation of PSs in electrolyte and exacerbates the PS shuttling effect. To combat this effect, herein we used heteroatom-doped HGF as a model system for electrocatalytically tailoring SRR kinetics. Within this model system consisting of nitrogen and sulfur dual-doped HGF (N,S-HGF) and non-doped or single-doped counterparts, the N,S-HGF exhibits superior SRR catalytic activity with considerably improved kinetics, including the highest exchange current density, the highest electron transfer number, the lowest interfacial charge transfer resistance and the lowest activation energy. Density functional theory (DFT) calculations reveal that the edge carbon atoms adjacent to the heteroatoms serve as the catalytic centers for SRR, and nitrogen and sulfur dual-doping tunes the *p*-orbital energy of the active carbon atoms to achieve an optimal LiS radical adsorption, minimizing the overpotential. Exploiting the unique SRR electrocatalytic performance, the N,S-HGF based electrodes exhibit much improved rate capability and cycling stability, suggesting the electrocatalytic approach represents a promising strategy to tackle the fundamental challenges facing Li-S batteries.

Results

Activation energy barrier in PS evolution

Sulfur reduction reaction in Li-S chemistry involves multi-step evolution of LiPSs during the discharge process. S_8 ring molecules first react with Li ions to form long-chain Li_2S_8 at ~2.7-2.4 V vs. Li/Li^+ electrode and then, through successive cleavage of S-S bonds, transform into a series of shorter chain LiPSs. The moieties include Li_2S_6 at 2.3 V, Li_2S_4 at 2.1 V, and finally the formation of insoluble Li_2S_2 and Li_2S products at ~2.1-1.7 V[19,20] (Fig. 1a,b). The initial cleavage of S_8 ring molecules is regarded as a relatively easy process, while the subsequent cleavage into shorter chain LiPSs becomes more and more difficult, and the last steps of the conversion into insoluble products are particularly slow[21,22]. The SRR kinetics at each step may be fundamentally represented by the activation energy. To this end, we have experimentally determined the activation energy (E_a) for each step of the PS conversion process by probing the charge transfer resistance at the corresponding voltages under various temperatures in a standard Ketjen carbon black/sulfur (KCB/S) composite cathode (1 mg cm^{-2}) (Fig. 1c,d). To stabilize the voltage for a specific conversion step, the cell was discharged to the desired potential and held at the same potential (chronoamperometry) until the output current remained constant. Then, electrochemical impedance spectroscopy (EIS) was

performed at 100 mV intervals from 2.7 V to 1.7 V in a frequency range from 10 mHz to 100 kHz with an AC amplitude of 5 mV.

Supplementary Fig. 1 shows the simplified-contact-Randles equivalent circuit fitting EIS of the device, where the first semicircle is attributed to the deposition of the insoluble Li_2S_2/Li_2S on the surface (R_{surf}), and the second semicircle is attributed to the charge transfer process (R_{CT}) in the KCB/S cathode[23]. By fitting the charge transfer resistance measured at different temperatures into an Arrhenius equation (Fig. 1c,d), we can derive the activation energy at each measurement voltage. Overall, the resulting E_a (Fig. 1e) shows a low value of 0.12 eV at 2.7 V (corresponding to the initial step conversion from S_8 to Li_2S_8), which increases to 0.24 eV at 2.4-2.1 V (corresponding to the conversion from Li_2S_8 to Li_2S_6 and Li_2S_4), and then reaches a maximum value of 0.33 eV at 1.8 V (for the final conversion into insoluble products). These activation energy studies clearly demonstrate that the conversion of the S_8 ring molecules to soluble LiPSs is relatively easy while the conversion of LiPSs into the final insoluble products is more difficult and represents the rate-determining step for practical Li-S batteries. Since most LiPSs (occurring at 2.7 V, 2.3 V and 2.1 V) are soluble in the electrolyte, the slow conversion of such soluble LiPS intermediates into insoluble final products leads to accumulation of LiPSs in the electrolyte and thus is primarily responsible for the PS shuttling effect and rapid capacity fading. To this end, designing proper electrocatalysts that can lower such energy barriers and accelerate the conversion of soluble LiPS intermediates into insoluble Li_2S_2/Li_2S, may offer an attractive approach that directly addresses the root cause of the PS shuttling challenge.

Rational design of heteroatom-doped HGF catalysts

We chose a series of heteroatom-doped holey graphene frameworks (HGFs) as model catalysts to explore electrocatalytic SRR. The materials include the pristine HGF, nitrogen-doped, sulfur-doped, and nitrogen and sulfur dual-doped HGFs (N-HGF, S-HGF, and N,S-HGF, respectively). A typical hydrothermal process (see Methods) was used to synthesize a 3D hierarchical HGF architecture with continuous graphene network structure for excellent electron transport, and fully interconnected micropores and nanopores for efficient mass transport and Li^+ diffusion (Fig. 2a,b and Supplementary Fig. 2)[24,25]. The holey graphene structure also provides abundant edge sites for heteroatom incorporation. It is known that the edge sites in the graphene oxide matrix are active for various functionalizations due to the structural inhomogeneity[26,27]. The hydrothermal or thermal annealing process may be used for

incorporating selected heteroatoms at the edge sites while retaining the sp^2-bonded carbon basal plane.

The chemical compositions and the bonding structures between the dopants and carbons in the heteroatom-doped HGF were characterized by X-ray photoelectron spectroscopy (XPS). An XPS survey scan of the N,S-HGF samples (Supplementary Fig. 3a) clearly showed the distinct peaks for N (~400 eV) and S (~164.5 and 228.2 eV), demonstrating the successful doping of N and S in graphene. The dopant contents in the samples can be estimated from the XPS survey results. The atomic ratios of N and S dopants in N,S-HGF are around 2.6 at. % and 2.3 at. %, respectively. High-resolution XPS spectra of the nitrogen elements in N,S-HGF may be deconvoluted into three peaks at 398.6 eV, 399.7 eV, and 401.2 eV (Fig. 2c), which may be attributed to pyridinic N, pyrrolic N and graphitic N, respectively. Sulfur atoms primarily form the thiophene-S-type C-S-C bonds, as validated by the XPS peaks at 163.6 and 164.7 eV (Fig. 2d), with a minor amount of sulfate and sulfide groups[28]. XPS characterizations for the single-doped counterparts were also conducted for comparison (Supplementary Fig. 3).

The bonding structures in the heteroatom-doped HGF can also be directly verified by annular dark-field scanning transmission electron microscopy (ADF-STEM). It can be clearly observed that the sulfur atoms (the bright dots in Fig. 2e) are only bonded with the carbon atoms in the form of thiophene-S-type bonds (Fig. 2f) at the edge sites of the nanopores (~1-2 nm). However, the nitrogen dopant is not visible in the STEM image due to the very close atomic number and little elemental contrast between N and C. The ADF-STEM characterizations can also provide helpful insights for the structural model constructions in our DFT calculations.

Activity, kinetics and mechanism of electrocatalytic SRR

To experimentally explore the fundamental electrocatalytic behavior of the heteroatom-doped HGFs for SRR, we carried out a series of electrochemical measurements including linear sweep voltammetry (LSV) and EIS, in combination with rotating disk electrode (RDE) measurements following the protocols well-developed in oxygen reduction reaction (ORR) community[29]. Prior to the LSV experiments, the N,S-HGF electrode was activated by cyclic voltammetry (CV) for 50 cycles at 10 mV s^{-1} in the non-faradaic range to reach a stable electrochemical active surface area (ECSA, Supplementary Fig. 4). Fig. 3a shows the SRR polarization curves of different heteroatom-doped HGF samples deposited on glassy carbon electrode (GC, geometric area of the GC electrode is 0.196 cm^2). In general, the SRR LSV

curve exhibits similar features to those of ORR including an onset potential, diffusion-limited current (J_D) and half-wave potential ($E_{1/2}$). The $E_{1/2}$ for the N,S-HGF was 2.22 V, which is considerably higher than those of N-HGF (2.05 V), S-HGF (2.03 V) and pristine HGF (2.00 V), respectively, suggesting an overall lower overpotential for the N,S-HGF.

The use of LSV curves to determine the Tafel slope (η) and exchange current density (J_0) provides the key kinetic parameters that characterize the reaction kinetics and catalytic activity of a given electrocatalyst. Smaller η and higher J_0 are important indications of faster reaction kinetics[30-33]. Notably, N,S-HGF catalysts exhibited the smallest Tafel slope of 80 mV dec^{-1}, compared with 157, 188 and 274 mV dec^{-1} for N-HGF, S-HGF and pristine HGF (Fig. 3b), indicating considerably accelerated reaction kinetics and higher electrocatalytic activity. Extrapolating the Tafel plot to zero overpotential gives the exchange current density (J_0) of 0.12 mA cm^{-2} for the N,S-HGF catalyst (Supplementary Discussion), which is higher than that obtained in the other samples (0.10 mA cm^{-2} for N-HGF, 0.09 mA cm^{-2} for S-HGF and 0.07 mA cm^{-2} for HGF, respectively).

The diffusion-limited current density (J_D) for the N,S-HGF is also considerably higher than the N-HGF, S-HGF, and pristine HGF catalysts. J_D is dependent on the active mass loading on the GC electrode, and reaches a peak at a mass loading of 0.1 mg cm^{-2} (Supplementary Fig. 5a). To understand the SRR mechanism with the presence of catalysts, the electron transfer numbers in the SRR process were calculated by using the J_D according to the Koutecky-Levich (K-L) equation (Supplementary Discussion) [34]. The K-L plots of N,S-HGF catalysts (Supplementary Fig. 5b), i.e., J^{-1} vs. $\omega^{-1/2}$, show excellent linearity, suggesting first-order reaction kinetics for the reduction of sulfur molecules dissolved in the electrolyte. The slopes of the K-L plots give electron transfer numbers for the SRR catalyzed by different materials. The N,S-HGF catalyst exhibits an apparent electron transfer number of ~7.8, suggesting an 8-electron reduction process with a theoretical conversion of S_8 into S_8^{8-} (equivalent to $4S_2^{2-}$). In contrast, the electron transfer numbers of N-HGF, S-HGF, and pristine HGF can be calculated as ~5.9, ~4.6 and ~3.3, respectively (Fig. 3c). The larger electron transfer number observed with the N,S-HGF catalyst suggests that it can promote more complete sulfur reduction and more rapid conversion of LiPS into the insoluble products, while the single-doped catalysts can only convert S_8 molecules into a mixture of both high-order and low-order LiPSs, and the pristine HGF catalyst can only reduce S_8 molecules into high-order

Li_2S_4. These analyses clearly suggest that N,S-HGF is a much more effective catalyst at driving the reduction of S_8 molecules into solid-state products as indicated by the RDE measurements.

To further understand the origin of the improved catalytic activity and kinetics of N,S-HGF catalyzed SRR, we have conducted EIS measurements at the onset potential (where the SRR just starts) to probe the charge transfer resistance. Charge transfer is an essential step where ions and electrons are transferred to the active centers in order to participate in the reaction. Therefore, the charge transfer kinetics at the catalyst-adsorbate interface represents the primary factor determining the electrocatalytic SRR kinetics[35]. The EIS curves (Fig. 3d and Supplementary Fig. 6a) show that the N,S-HGF catalysts exhibit the smallest charge transfer resistance (2.5 $\Omega \cdot cm^2$) during SRR in comparison to those of N-HGF (7.0 $\Omega \cdot cm^2$), S-HGF (12.9 $\Omega \cdot cm^2$) and pristine HGF (15.4 $\Omega \cdot cm^2$), suggesting superior charge transfer kinetics.

We extended these EIS measurements and determined the temperature dependence of charge transfer resistance at the onset potential. This enabled us to extract the activation energy E_a by using the Arrhenius equation (Supplementary Fig. 6b)[36]. The logarithmic values of the reciprocal of the charge transfer resistance obeyed a linear relationship with the inverse of the absolute temperatures (Fig. 3e). Following the Arrhenius relation, we determined the activation energy (E_a) to be 0.06 eV for N,S-HGF, 0.09 eV for N-HGF, 0.15 eV for S-HGF and 0.23 eV for pristine HGF (Fig. 3f). Having the lowest activation energy is consistent with the superior kinetics of N,S-HGF for electrocatalytic SRR.

Theoretical modeling of the activity origin on SRR

To better understand the fundamental origins of the SRR catalytic activity of the heteroatom-doped HGFs, we carried out DFT calculations to elucidate how heteroatom doping affects the catalytic activity. The fundamental SRR process for the catalysts involves a series of reduction reactions that progress from S_8 ring molecules to the final product of Li_2S ($S_8 \rightarrow Li_2S_8 \rightarrow Li_2S_6 \rightarrow Li_2S_4 \rightarrow Li_2S_2 \rightarrow Li_2S$) following four basic steps (diffusion, adsorption, reaction and desorption). It is generally believed that a moderate adsorption, not too strong or too weak, of the adsorbate on the catalytic sites is the key prerequisite for an efficient electrocatalyst. As inspired by the research on heteroatom-doped carbon materials for ORR, the carbon atoms adjacent to the heteroatoms are the preferential binding sites for the sulfur intermediates rather than the heteroatoms themselves due to the charge redistribution induced by the heteroatom doping[37]. Indeed, our calculations indicate that the adsorption energy of the PS intermediates on carbon atoms of the basal plane is too weak and that on the heteroatoms is

too strong (Supplementary Fig. 7). Therefore, the carbon atoms adjacent to the heteroatoms provide the optimal adsorption sites and are the most probable active sites for the catalytic SRR process.

Since the final reaction ($Li_2S_2 + 2Li^+ + 2e^- \rightarrow 2Li_2S$) represents the rate-determining step with considerably larger E_a than the other conversion steps, we focus our calculations on the final two-electron process as we investigate the catalytic properties of different possible structures (Supplementary Discussion). We assumed that the conversion of Li_2S_2 to Li_2S undergoes a step reaction involving the formation of a LiS radical intermediate, solvated by the 1,3-dioxolane (DOL) solvent and interacting with the catalytic active site. Unlike previous theoretical models that only dealt with the ideal case where the Li^+ ion was located in a vacuum state without considering the solvation by the electrolyte solvents[38,39], we constructed a microsolvation state model which is closer to the practical conditions (Fig. 4a). In this approach we consider the Li^+ ion in LiS as solvated by 3 explicit DOL molecules, and the ensemble is placed in an implicit continuum solvent model of dielectric constant 7.0. The microsolvated LiS intermediate interacting with the active site (*) is denoted as 3DOL-LiS*, as expressed in the following equations:

$$3DOL + Li_2S_2 + Li^+ + e^- + * \rightarrow 3DOL\text{-}LiS* + Li_2S \quad (1)$$

$$3DOL\text{-}LiS* + Li^+ + e^- \rightarrow Li_2S + * + 3DOL \quad (2)$$

Due to the strong cation nature of Li^+, the microsolvation approach of combining explicit and implicit solvent serves as an effective approach for correctly describing the solvation of the reactant (Supplementary Fig. 8).

According to equations (1) and (2), the adsorption Gibbs free energy of LiS* ($\Delta G(LiS*)$) on the active sites can be expressed in equation (3) and the Gibbs free energy (ΔG) of the final two steps can be written as a function of $\Delta G(LiS*)$:

$$\Delta G(LiS*) = G(3DOL\text{-}LiS*) - G(*) + G(Li) - G(Li_2S) - 3G(DOL) \quad (3)$$

$$\Delta G_1 = \Delta G(LiS*) \quad (4)$$

$$\Delta G_2 = -\Delta G(LiS*) + 2G(Li_2S) - 2G(Li) - G(Li_2S_2) \quad (5)$$

The catalytic activity is closely related to the thermodynamic overpotential for the Li_2S_2 to Li_2S conversion reaction, which appears in a volcano plot as a function of $\Delta G(LiS*)$ when catalyzed at different catalytic sites, with special sites reaching the optimal value[40]. $\Delta G(LiS*)$

for carbon atoms on the basal plane of graphene are in the region of weak adsorption. This is because the distortion of C-C bonds induced by the carbon hybridization change from sp^2 to sp^3 requires too much energy that cannot be compensated by the C-S bond formation during the catalytic SRR process. The edge carbon atoms, however, provide the opportunity to show reasonable adsorption energy as the distortion is much easier. In this regard, the carbon atoms located at the armchair edge, zigzag edge and inner defect edge were considered as various active sites to analyze the adsorption energy and the catalytic activity (Fig. 4a). Notably, the O/OH group on the zigzag/armchair/defective models is verified not to benefit to generate structures with reasonable stability and improved catalytic properties (Supplementary Table 1).

Governed by the Sabatier principle, the relationship between the overpotential and the adsorption energy displays a volcano shape (Fig. 4b), where several edge carbon sites on the N,S-HGF catalyst and on the N-HGF, S-HGF and HGF catalyst models (Supplementary Fig. 9) are compared. For the structures on the left side, the potential limiting step is step (1) whereas on the right side of the volcano, the potential is limited by reaction step (2). Perfect nondoped graphene presents sites that bind LiS either too strongly like on the zigzag edge (-3.00 eV) or too weakly like on the armchair edge (-1.73 eV), and thus they are intrinsically bad catalytic sites. As for the inner defective nondoped HGF, the edge carbon atoms show a hybrid geometry between armchair and zigzag edges. This structure results in a favorable adsorption energy of -2.14 eV, presenting a good compromise of LiS binding and consequently a low overpotential. Moreover, N,S dual-doping further provides finer tuning, pushing the N,S-HGF system almost at the top of the volcano plot and further decreasing the overpotential to a negligible value. The adsorption energy calculation results can be experimentally verified by the PS-adsorption experiments (Supplementary Fig. 10).

In order to unravel the origin of the high catalytic SRR activity, we considered the doping process as an approach to engineering the *p*-orbital of the catalytic sites and thereby the catalytic performance (Fig. 4c). Inspired by the *d*-band center theory for metallic catalysts[41], we used the *p*-band center for the density of states projected on the active carbon as a descriptor of the electronic structure of the heteroatom-doped catalysts and found a relationship with the adsorption energy of LiS (Fig. 4d). Before adsorption, the valence *p*-band in the projected density of states (pDOS) of the S atom in the LiS radical shows an isolated feature. After adsorption on the catalysts, a significant change to the pDOS shape of the valence *p*-band arises from the bonding with the *p*-orbital of the catalytic carbon atoms (Supplementary Fig. 11). The

bonding strength, according to classical bonding theory, is related to the energy gap between these bonding orbitals: as the *p*-orbital of S atom in LiS radical can be considered at constant position, tuning the position of the *p*-orbital of catalytic carbon atoms to manipulate the adsorption can be achieved by heteroatom doping. N-S dual-doping generally provides an intermediate *p*-band center energy, hence a moderate bonding strength with the LiS radical, thus leading to the optimal catalytic activity. The *p*-band center also provides an opportunity to estimate the performance of different sites without the demanding calculation of the adsorbed structure. In addition to the *p*-band theory, other factors that may influence the catalytic activity, such as charge, dipole and strain effect, have also been discussed (Supplementary Figure 12), and the results show that the correlation between these factors and the adsorption energy is not significantly better than the *p*-band center.

SRR in Li-S battery

While previous RDE measurements (Fig. 3) demonstrated superior electrocatalytic SRR activities for N,S-HGF catalysts in an open cell environment, it is of practical importance to evaluate the effect of electrocatalysis on device performance. Accordingly, we systematically explored the activation energy profiles and overall performance of the heteroatom-doped HGF cathodes in Li-S coin cells. First, we conducted the same activation energy measurements by determining the temperature-dependent EIS curves at various voltages (Supplementary Fig. 13) to verify that selected catalysts are capable of accelerating the LiPS conversion particularly the rate-determining step. The EIS curves of different HGF catalysts show similar behavior to that of KCB/S cathode, and among them the N,S-HGF catalyst exhibits the smallest charge transfer resistance. Fig. 5a shows the E_a profiles at various voltages for the four different catalyst based cathodes (loading of 1 mg cm^{-2}). Overall, the activation energy for non-doped HGF displays a similar stepwise profile to that of the control device made from the standard KCB/S composite cathode (see Fig. 1e). That is, there are relatively low E_a values at the initial-reduction stage (~2.7-2.5 V) which increase at the median-reduction stage (~2.4-2.0 V) and peak at the final-reduction stage (~1.9-1.7 V), again confirming that the last steps of conversion into insoluble Li_2S_2/Li_2S products are the rate-determining steps. With the introduction of heteroatom dopants, the activation energies are reduced considerably, especially for final rate-determining step. Overall, the activation energies follow a similar trend to that observed in RDE studies in that the values decrease in the order from HGF, S-HGF, N-HGF, to N,S-HGF.

In particular, the maximum activation energy is decreased from >0.32 eV in HGF to 0.12 eV in N,S-HGF electrodes for the final LiPS conversion into insoluble Li_2S_2/Li_2S.

The different E_a values for the four heteroatom-doped HGFs can also account for the different polarization voltage gaps (Fig. 5b,c). As shown in Fig. 5b, N,S-HGF exhibited the smallest polarization voltage gap (152 mV) between anodic and cathodic sweep among the four different samples at the current density of 0.2 C. Moreover, since a larger current density would induce more severe polarization and larger voltage gaps, because of the considerably better catalytic activity and lowered E_a for the N,S-HGF catalyst, the increase in voltage gap from 0.05 C to 2 C is only 130 mV (from 140 mV to 270 mV). This value is considerably lower than those of N-HGF (210 mV), S-HGF (370 mV) and non-doped HGF (541 mV) catalysts (Fig. 5c and Supplementary Fig. 14).

To directly evaluate the impact of the electrocatalysts in battery performance, we have further compared the rate capability and cycling behavior of the Li-S coin cell assembled with different catalysts. For a sulfur mass loading of 4 mg cm^{-2}, the N,S dual-doped HGF electrodes exhibited excellent rate capability, delivering specific capacities of 1390, 840 and 577 mAh g^{-1} at 0.1 C, 1 C and 2 C, respectively (Fig. 5d). In contrast, with lower catalytic activity, the N-HGF, S-HGF, and pristine HGF displayed considerably lower capacity, especially at high rate. Furthermore, the acceleration of PS conversion into solid Li_2S_2/Li_2S reduces the PS accumulation and thus effectively mitigates the PS shuttling effect, leading to improved cycling stability. The N,S dual-doped HGF electrodes displayed an extremely low capacity decay of 0.025%/cycle at 1 C for 500 cycles, compared to of 0.054%/cycle, 0.098%/cycle, and 0.162%/cycle for the N-HGF, S-HGF, and pristine HGF, respectively (Fig. 5e). Such comparisons clearly highlight the greatly enhanced performance resulted from the improved SRR catalytic activity.

In summary, we have conducted a systematic investigation of SRR kinetics by directly profiling the activation energies in the multi-step SRR process. We reveal that the initial reduction of S_8 ring molecules to the soluble PSs is relatively easy with low activation energy, while the subsequent conversion of the PSs into the insoluble Li_2S_2/Li_2S is more difficult with much higher activation energy, which fundamentally contributes to the accumulation of PSs in electrolyte and exacerbates the PS shuttling effect. Heteroatom-doped graphene was used as a model system to demonstrate that the electrocatalytic strategy can accelerate the PS conversion kinetics and mitigate the PS shuttling effect. Experimental results and theoretical calculations

establish that dual-doped N,S-HGF exhibited superior electrocatalytic SRR activity with considerably lower charge transfer resistance and a greatly reduced activation energy, leading to Li-S cells that exhibit significant improvements in rate capability and cycling stability. These studies establish that electrocatalytic SRR is a promising pathway to highly robust Li-S batteries. Beyond the heteroatom model system described in current study, the same approach can be applied to many other potential SRR electrocatalysts, including single transition metal atom catalysts[42], metal oxides or metal sulfides[43].

Methods

Synthesis of graphene oxide and heteroatom-doped holey graphene framework. GO was prepared according to a modified Hummers' method[44]. Briefly, 6 g natural graphite (325 mesh, Sigma Aldrich) was added into 140 mL concentrated sulfuric acid under vigorous stirring in an ice-water bath, followed by slowly adding 3 g sodium nitrate (Sigma Aldrich) and 18 g potassium permanganate (Sigma Aldrich). Due to the strong acidity of sulfuric acid and strong oxidizability of the sodium nitrate and potassium permanganate, it is necessary to keep the temperature near 0 °C to avoid the fast oxidation of the graphite and any kinds of unsafe accidents. After stirring for 30 mins, the reaction system was transferred into a water-bath at ~50 °C, and was kept stirring till the mixture forming a thick paste. Successively, the system was transferred back to the ice-water bath, followed by drop-wisely adding ~1L iced D.I. water. The mixture was then centrifuged and washed by using 1:10 HCl aqueous solution for three times followed by repeated washing with D.I. water. The final solution was dialyzed for one week to remove the extra H^+ ions absorbed on the GO surfaces. Heteroatom-doped HGFs were synthesized by reacting the dopant sources with the holey graphene oxide (HGO) aqueous dispersion through a typical hydrothermal method. HGO aqueous dispersion was synthesized according to our previous method[24], by mixing 50 mL of 2 GO mg mL^{-1} GO aqueous dispersion solution with 5 mL of 30% H_2O_2 aqueous solution at 100 °C under stirring for 2 hours. Specifically, 10 mmol of NH_4SCN powders were added into the 10 mL of 2 mg ml^{-1} HGO dispersion, followed by magnetic stirring and sonication for 2 hours to dissolve the NH_4SCN thoroughly. The mixed dispersion was then transferred into an autoclave and heated at 180 °C for 6 hours. After the hydrothermal treatment, a freestanding nitrogen and sulfur dual-doped holey graphene framework (N,S-HGF) hydrogel can be obtained. The hydrogel was then freeze-dried and annealed at 900 °C for 1 hour to obtain the N,S-HGF aerogel[45]. The control samples, namely N-HGF, S-HGF and pristine HGF, were synthesized by changing the dopant source into urea and Na_2S, or without dopant sources, following the same procedures. To be noted, the dopant concentration of each catalyst has been optimized prior to the final presentation. The results presented in the manuscript are based on the optimized samples with the best electrochemical performance and structural integrity simultaneously.

Preparation of the electrolyte and Li_2S_6 catholyte. The electrolyte (denoted as blank electrolyte) was made of 1 M lithium bis(trifluoromethanesulfonyl)imide (LiTFSI, Sigma Aldrich) and 0.2 M lithium nitrate ($LiNO_3$, Sigma Aldrich) in the Dimethoxyethane (DME, Sigma Aldrich) and 1,3-Dioxolane (DOL, Sigma Aldrich) mixed solution (1:1 by volume). The Li_2S_6 catholyte (1 M) was prepared by reacting the sublimed sulfur (Sigma Aldrich) with Li_2S (Sigma Aldrich) in stoichiometric proportion in the blank electrolyte. The mixture was vigorously stirred at 50 °C in an Ar-filled glove box overnight to produce a brownish-red Li2S6 catholyte solution. The PS-adsorption test was conducted by immersing 3 mg of the heteroatom-doped HGF catalysts in 3 mL of 10 mM Li_2S_4 solutions at room temperature for 24 hours.

Electrochemical measurements. The electrocatalytic sulfur reduction reaction (SRR) activity was tested by using a CHI 760E electrochemical workstation (CH Instruments, Shanghai, China) coupled with the rotating disc electrode (RDE) technique (Pine Research Instrumentation, USA) in an Ar-filled glovebox. 10 µL of 2 mg mL^{-1} catalyst ink (made by sonicating 2 mg catalysts in 1 mL ethanol and 20 µL 5 wt% Nafion solution) was drop-cast onto a freshly polished glassy carbon (GC) electrode (0.196 cm^2) to form a flat film electrode with an areal mass loading of 0.1 mg cm^{-2} (for all catalysts). The electrochemical test was performed in a two-electrode open-cell located in the glovebox, by using Li foil as the counter and reference electrode and the catalyst film as working electrode. The electrolyte solution used for SRR tests was 4 mM S_8 molecules dissolved in the blank electrolyte. Prior to the SRR electrocatalysis test, the catalyst film electrode was firstly activated in the blank electrolyte by scanning the CV in the range of 3.1 V to 3.0 V for 50 cycles at 10 mV s^{-1}. Then, LSV measurement was conducted in the S_8 solution with the sweep rate of 20 mV s^{-1} in the voltage range of 3.3 V to 1V. Meanwhile, the LSV curve in the blank electrolyte should also be recorded as the background curve, which is used to obtain the realistic LSV profile of SRR.

The overall electrochemical performance of the catalyst was conducted in the CR2032 coin cells assembled in an Ar-filled glovebox. The catalyst electrode was prepared by directly pressing the aerogel into a freestanding thin film, and the mass of the thin film can be controlled by tuning the height of the aerogel. Afterwards, Li_2S_6 catholyte was directly used as sulfur source to drop cast in the catalyst electrode. In our experiment, we set the mass ratio of the sulfur in the cathodes as 67% unless otherwise specified. The sulfur cathodes were then directly assembled into a CR2032 coin cell with Li foil, Celgard 2500 separator and blank electrolyte (E/S ratio = 5/1 μL/mg). Cyclic voltammetry (CV) curves were recorded in the voltage range of 1.7 V ~ 2.7 V at the scanning rate of 0.2 mV s^{-1}. The charge/discharge curves were tested in the voltage range of 1.7 V ~ 2.7 V at various C rates (1 C = 1670 mAh g^{-1}), and rate capability was evaluated by testing the capacity at 0.1 C, 0.2 C, 0.5 C, 1 C and 2 C. Electrochemical impedance spectroscopy (EIS) tests was performed at specific voltage values in the frequency range of 1 MHz to 0.01 Hz with an amplitude of 5 mV. A Linkam stage (HFSX350) was used to control the temperature during the activation energy measurements.

Material characterizations. The morphology and structure of the resulting materials were characterized by SEM (Zeiss Supra 40VP), XPS (Kratos AXIS Ultra DLD spectrometer) and Raman spectroscopy (RM 2000 Microscopic confocal Raman spectrometer Horiba LABHR using a 488 nm laser beam). ADF STEM imaging was performed on an aberration-corrected JEOL ARM300CF STEM equipped with a JEOL ETA corrector operated at an accelerating voltage of 80 kV located in the electron Physical Sciences Imaging Centre (ePSIC) at Diamond Light Source. ADF imaging was performed at 80 keV with a CL aperture of 30 μm, convergence semiangle of 24.8 mrad, beam current of 12 pA, and acquisition angle of 27–110 mrad.

Characterizations. Characterizations were carried out using scanning electron microscopy (SEM, JEOL JSM-6700F FE-SEM) with energy dispersive spectroscopy (EDAX), transmission electron microscopy (TEM, T12 Quick CryoEM and CryoET FEI; acceleration voltage, 120 KV. Titan S/TEM FEI; acceleration voltage, 300 KV), X-ray diffraction (XRD, Panalytical X'Pert Pro X-ray Powder Diffractometer), atomic force microscopy (AFM, Bruker Dimension Icon Scanning Probe Microscope), UV-Vis-NIR spectroscopy (Shimadzu 3100 PC), Raman and PL spectroscopy (Horiba, 488 nm laser wavelength), and X-ray photoelectron spectroscopy (XPS, AXIS Ultra DLD). For the PL spectra collection, exfoliated monolayer MoS_2 nanosheets after the TFSI treatment were used. The transport characteristic measurements were conducted at room temperature under ambient conditions (in vacuum and dark) with a probe station and a computer-controlled analogue-to-digital converter.

DFT calculations. Major parts of calculations are performed with density-functional theory (DFT)[46] using the Vienna Ab initio Simulation Package (VASP)[47]. Perdew–Burke-Ernzerhof (PBE)[48] functional at the generalized gradient approximation (GGA) level. Cutoff energy of basis set is 500 eV cutoff as required by the Li_sv pseudopotential to give a reasonable description of Li related species. The dDsC dispersion correction is applied[49,50]. Solvation effects are described using an implicit dielectric model as implemented in the VaspSol[51] addon package. The cavitation energy contribution is neglected for numeric stability. The accuracy is set to be ACCURATE as recommend by VaspSol. All calculations are spin-polarized.

Data availability

The data that support the findings of this study are available from the corresponding author on reasonable request.

References

1. Manthiram, A., Fu, Y., Chung, S.-H., Zu, C. & Su, Y.-S. Rechargeable lithium–sulfur batteries. *Chem. Rev.* **114**, 11751-11787 (2014).

2. Pang, Q., Liang, X., Kwok, C. Y. & Nazar, L. F. Advances in lithium–sulfur batteries based on multifunctional cathodes and electrolytes. *Nat. Energy* **1**, 16132 (2016).

3. Mikhaylik, Y. V. & Akridge, J. R. Polysulfide shuttle study in the Li/S battery system. *J. Electrochem. Soc.* **151**, A1969-A1976 (2004).

4. Ma, L., Hendrickson, K. E., Wei, S. & Archer, L. A. Nanomaterials: Science and applications in the lithium–sulfur battery. *Nano Today* **10**, 315-338 (2015).

5. Seh, Z. W., Sun, Y., Zhang, Q. & Cui, Y. Designing high-energy lithium–sulfur batteries. *Chem. Soc. Rev.* **45**, 5605-5634 (2016).

6. Bonaccorso, F. *et al.* Graphene, related two-dimensional crystals, and hybrid systems for energy conversion and storage. *Science* **347**, 1246501 (2015).

7. Guo, B. *et al.* Highly dispersed sulfur in a porous aromatic framework as a cathode for lithium–sulfur batteries. *Chem. Comm.* **49**, 4905-4907 (2013).

8. Li, L. *et al.* Stabilizing sulfur cathodes using nitrogen-doped graphene as a chemical immobilizer for LiS batteries. *Carbon* **108**, 120-126 (2016).

9. He, J. *et al.* Freestanding 1T MoS_2/graphene heterostructures as a highly efficient electrocatalyst for lithium polysulfides in Li–S batteries. *Energy Environ. Sci.* **12**, 344-350 (2019).

10. Peng, L., Zhu, Y., Chen, D., Ruoff, R. S. & Yu, G. Two-dimensional materials for beyond-lithium-ion batteries. *Adv. Energy Mater.* **6**, 1600025 (2016).

11. Cui, Z., Zu, C., Zhou, W., Manthiram, A. & Goodenough, J. B. Mesoporous titanium nitride-enabled highly stable lithium-sulfur batteries. *Adv. Mater.* **28**, 6926-6931 (2016).

12. Wang, D. *et al.* A general atomic surface modification strategy for improving anchoring and electrocatalysis behavior of $Ti_3C_2T_2$ MXene in lithium–sulfur batteries. *ACS Nano* **13**, 11078-11086 (2019).

13. Zheng, J. *et al.* lewis acid–base interactions between polysulfides and metal organic framework in lithium sulfur batteries. *Nano Lett.* **14**, 2345-2352 (2014).

14. Ji, X. & Nazar, L. F. Advances in Li-S batteries. *J. Mater. Chem.* **20**, 9821-9826 (2010).

15. Bruce, P. G., Freunberger, S. A., Hardwick, L. J. & Tarascon, J.-M. Li-O_2 and Li-S batteries with high energy storage. *Nat. Mater.* **11**, 19-29 (2012).

16. Du, Z. *et al.* Cobalt in nitrogen-doped graphene as single-atom catalyst for high-sulfur content lithium–sulfur batteries. *J. Am. Chem. Soc.* **141**, 3977-3985 (2019).

17. Xu, Z.-L. *et al.* Exceptional catalytic effects of black phosphorus quantum dots in shuttling-free lithium sulfur batteries. *Nat. Commun.* **9**, 4164 (2018).

18. Park, J. *et al.* Tungsten disulfide catalysts supported on a carbon cloth interlayer for high performance Li–S battery. *Adv. Energy Mater.* **7**, 1602567 (2017).

19. Wild, M. *et al.* Lithium sulfur batteries, a mechanistic review. *Energy Environ. Sci.* **8**, 3477-3494 (2015).

20. Barchasz, C. *et al.* Lithium/sulfur cell discharge mechanism: An original approach for intermediate species identification. *Anal. Chem.* **84**, 3973-3980 (2012).

21. Wang, L. *et al.* A quantum-chemical study on the discharge reaction mechanism of lithium-sulfur batteries. *J. Energy Chem.* **22**, 72-77 (2013).

22. Yin, Y.-X., Xin, S., Guo, Y.-G. & Wan, L.-J. Lithium–sulfur batteries: electrochemistry, materials, and prospects. *Angew. Chem. Int. Ed.* **52**, 13186-13200 (2013).

23. Tan, G. *et al.* Burning lithium in CS_2 for high-performing compact Li_2S–graphene nanocapsules for Li–S batteries. *Nat. Energy* **2**, 17090 (2017).

24. Sun, H. *et al.* Three-dimensional holey-graphene/niobia composite architectures for ultrahigh-rate energy storage. *Science* **356**, 599-604 (2017).

25. Xu, Y. *et al.* Holey graphene frameworks for highly efficient capacitive energy storage. *Nat. Commun.* **5**, 4554 (2014).

26. Duan, J., Chen, S., Jaroniec, M. & Qiao, S. Z. Heteroatom-doped graphene-based materials for energy-relevant electrocatalytic processes. *ACS Catal.* **5**, 5207-5234 (2015).

27. Zhou, H. *et al.* Understanding defect-stabilized noncovalent functionalization of graphene. *Adv. Mater. Interfaces* **2**, 1500277 (2015).

28. Wang, X. *et al.* Heteroatom-doped graphene materials: syntheses, properties and applications. *Chem. Soc. Rev.* **43**, 7067-7098 (2014).

29. Paulus, U. A., Schmidt, T. J., Gasteiger, H. A. & Behm, R. J. Oxygen reduction on a high-surface area Pt/Vulcan carbon catalyst: a thin-film rotating ring-disk electrode study. *J. Electroanal. Chem.* **495**, 134-145 (2001).

30. Suen, N.-T. *et al.* Electrocatalysis for the oxygen evolution reaction: recent development and future perspectives. *Chem. Soc. Rev.* **46**, 337-365 (2017).

31. Li, M. *et al.* Single-atom tailoring of platinum nanocatalysts for high-performance multifunctional electrocatalysis. *Nat. Catal.* **2**, 495-503 (2019).

32. Li, M. *et al.* Ultrafine jagged platinum nanowires enable ultrahigh mass activity for the oxygen reduction reaction. *Science* **354**, 1414-1419 (2016).

33. Lu, Y.-C., He, Q. & Gasteiger, H. A. Probing the lithium–sulfur redox reactions: A rotating-ring disk electrode study. *J. Phys. Chem. C* **118**, 5733-5741 (2014).

34. Zhou, R., Zheng, Y., Jaroniec, M. & Qiao, S.-Z. Determination of the electron transfer number for the oxygen reduction reaction: from theory to experiment. *ACS Catal.* **6**, 4720-4728 (2016).

35. Bazant, M. Z. Theory of chemical kinetics and charge transfer based on nonequilibrium thermodynamics. *Acc. Chem. Res.* **46**, 1144-1160 (2013).

36. Ogihara, N. *et al.* Theoretical and experimental analysis of porous electrodes for lithium-ion batteries by electrochemical impedance spectroscopy using a symmetric cell. *J. Electrochem. Soc.* **159**, A1034-A1039 (2012).

37. Li, M., Zhang, L., Xu, Q., Niu, J. & Xia, Z. N-doped graphene as catalysts for oxygen reduction and oxygen evolution reactions: Theoretical considerations. *J. Catal.* **314**, 66-72 (2014).

38. Zhou, G., Paek, E., Hwang, G. S. & Manthiram, A. Long-life Li/polysulphide batteries with high sulphur loading enabled by lightweight three-dimensional nitrogen/sulphur-codoped graphene sponge. *Nat. Commun.* **6**, 7760 (2015).

39. Ji, Z. *et al.* Anchoring lithium polysulfides via affinitive interactions: electrostatic attraction, hydrogen bonding, or in parallel? *J. Phys. Chem. C* **119**, 20495-20502 (2015).

40. Nørskov, J. K. *et al.* Origin of the overpotential for oxygen reduction at a fuel-cell cathode. *J. Phys. Chem. B* **108**, 17886-17892 (2004).

41. Hammer, B. & Nørskov, J. K. Why gold is the noblest of all the metals. *Nature* **376**, 238-240 (1995).

42. Fei, H. *et al.* Single atom electrocatalysts supported on graphene or graphene-like carbons. *Chem. Soc. Rev.* **48**, 5207-5241 (2019).

43. Wang, D. & Astruc, D. The recent development of efficient Earth-abundant transition-metal nanocatalysts. *Chem. Soc. Rev.* **46**, 816-854 (2017).

44. Xu, Y., Sheng, K., Li, C. & Shi, G. Self-assembled graphene hydrogel via a one-step hydrothermal process. *ACS Nano* **4**, 4324-4330 (2010).

45. Fei, H. *et al.* General synthesis and definitive structural identification of MN_4C_4 single-atom catalysts with tunable electrocatalytic activities. *Nat. Catal.* **1**, 63-72 (2018).

46. Kohn, W. & Sham, L. J. Self-consistent equations including exchange and correlation effects. *Phys. Rev.* **140**, A1133-A1138 (1965).

47. Kresse, G. & Hafner, J. Ab initio molecular dynamics for liquid metals. *Phys. Rev. B* **47**, 558-561 (1993).

48. Perdew, J. P., Burke, K. & Ernzerhof, M. Generalized gradient approximation made simple. *Phys. Rev. Lett.* **77**, 3865-3868 (1996).

49. Steinmann, S. N. & Corminboeuf, C. Comprehensive benchmarking of a density-dependent dispersion correction. *J. Chem. Theory Comput.* **7**, 3567-3577 (2011).

50. Steinmann, S. N. & Corminboeuf, C. A generalized-gradient approximation exchange hole model for dispersion coefficients. *J. Chem. Phys.* **134**, 044117 (2011).

51. Mathew, K., Sundararaman, R., Letchworth-Weaver, K., Arias, T. A. & Hennig, R. G. Implicit solvation model for density-functional study of nanocrystal surfaces and reaction pathways. *J. Chem. Phys.* **140**, 084106 (2014).

52. Towns, J. *et al.* XSEDE: Accelerating scientific discovery, *Comput. Sci. Eng.* **16**, 62-74, (2014).

Acknowledgments

This work is supported by the Center for Synthetic Control Across Length-scales for Advancing Rechargeables, an Energy Frontier Research Center funded by the US Department of Energy, Office of Science Basic Energy Sciences program under Award DE-SC0019381. Y.H. acknowledges the support by Office of Naval Research through grant number N00010141712608 (initial effort on catalyst preparation and rotating disc electrode electrochemical characterizations). I.M. and Z.A.A. acknowledge the support by the International Scientific Partnership Program (ISPP-147) at King Saud University. We acknowledge the Electron Imaging Center at UCLA for SEM technical support and the

Nanoelectronics Research Facility at UCLA for device fabrication technical support. We thank Diamond Light Source for access and support in use of the electron Physical Science Imaging Centre (MG23956). The calculations were performed on the Hoffman2 cluster at UCLA Institute for Digital Research and Education (IDRE), The National Energy Research Scientific Computing Center (NERSC), and the Extreme Science and Engineering Discovery Environment (XSEDE)[52], which is supported by National Science Foundation grant number ACI-1548562, through allocation TG-CHE170060.

Author contributions

X.D., Y.H. and L.P. conceived and designed the experimental research; P.S., and Z.W. designed and performed the DFT calculations; L.P. performed the experiments and conducted the data analysis with the contributions from C.W., J.L., Z.C., D.Z., D.B., H.L., X.X., I.S., Z.A.A., S.T., B.D., Y.H. and X.D.; C.S.A. and A.I.K. contributed to the TEM characterizations; All authors discussed the results and commented on the manuscript. **Competing interests:** The authors declare no competing interests.

Author Information

 Correspondence and requests for materials should be addressed to X.D. (xduan@chem.ucla.edu); P.S. (sautet@ucla.edu); Y.H. (yhuang@seas.ucla.edu)

Figure Captions

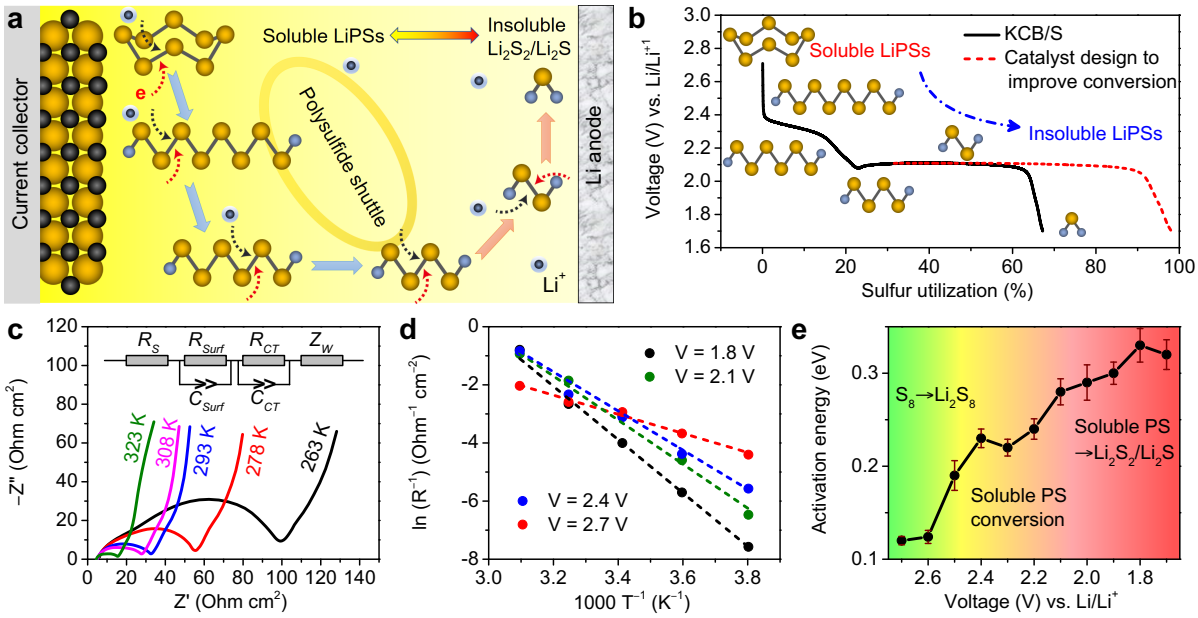

Fig. 1 | Activation energy in sulfur reduction and PS conversion reaction. a, Schematic illustration of SRR process involving the LiPS evolution. **b**, Discharge profile of the KCB/S cathode. The red dashed curve represents the expected LiPS conversion enhanced by catalyst design. **c**, EIS measurements at various temperatures at 2.7 V. Inset: simplified-contact-Randles equivalent circuit. **d**, Arrhenius plot showing linear relationship between logarithmic values of the reciprocal of charge transfer resistance and the reciprocal of absolute temperatures for 2.7 V, 2.4 V, 2.1 V and 1.8 V. **e**, Activation energy profiles at various voltages, highlighting the final step conversion of LiPSs into insoluble products is the rate-determining step and responsible for PS accumulation and shuttling. Error bars in **e** indicate the standard deviation of three independent electrodes.

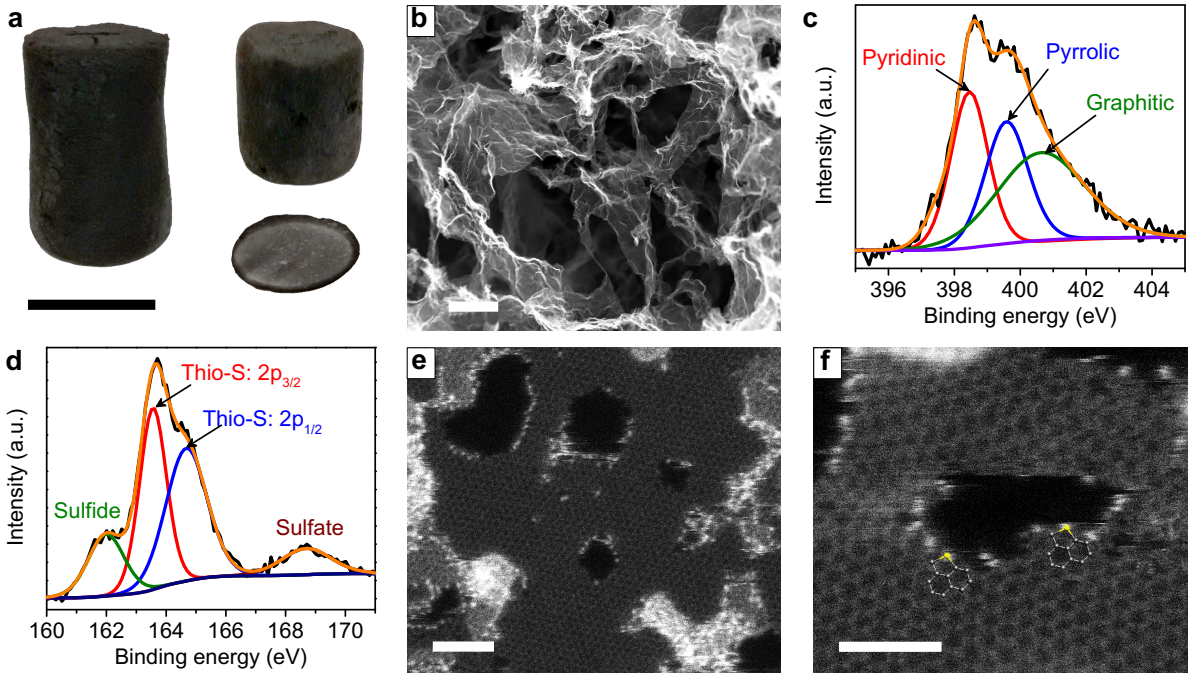

Fig. 2 | Material characterization of the N,S-HGF. a, Photograph of freestanding N,S-HGF

with different sizes and the corresponding thin film. Scale bar, 1 cm. **b**, SEM image of the N,S-HGF showing the hierarchical porous structure. Scale bar, 2 μm. **c**,**d**, High-resolution XPS spectra of N1s (**c**) and S2p (**d**). **e**, ADF-STEM images of N,S-graphene nanosheets showing the isolated pores and the location of sulfur dopants in the graphene matrix. Scale bar, 2 nm. **f,** Enlarged ADF-STEM image of N,S-graphene nanosheets. The bright dots represent the S dopant on the graphene plane, showing a thiophene-S-type bond structure. Scale bar, 1 nm.

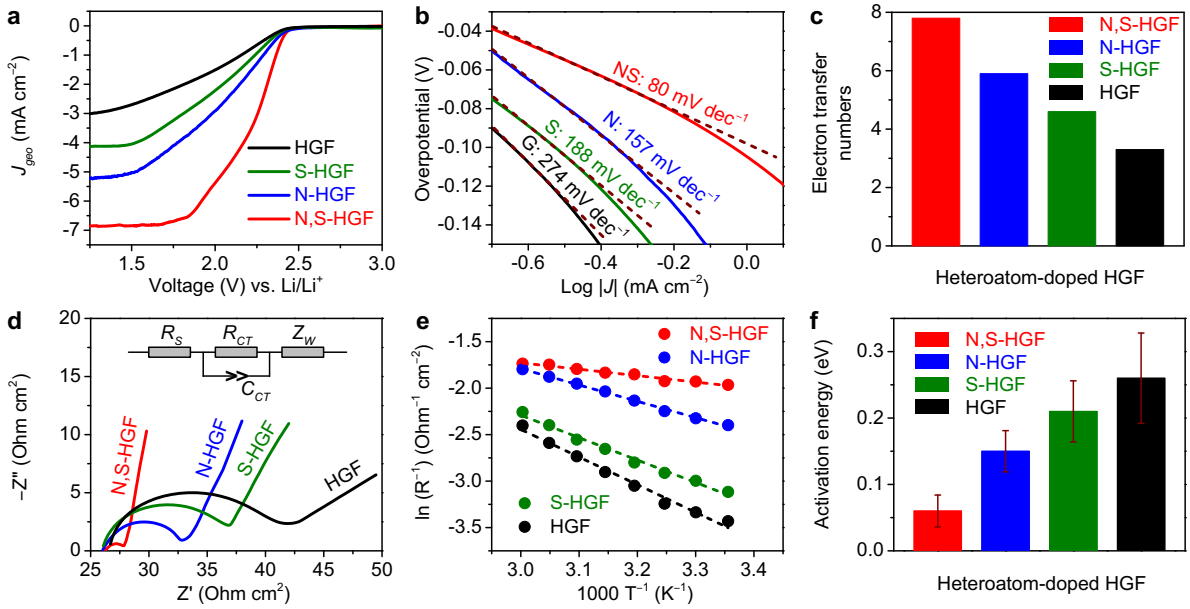

Fig. 3 | Catalytic SRR activity and kinetic analyses of heteroatom-doped HGFs in RDE. a, Linear sweep voltammetry (LSV) curves of heteroatom-doped HGFs towards sulfur reduction. **b**, Tafel plots of heteroatom-doped HGFs. **c**, Electron transfer number comparison among heteroatom-doped HGFs. **d**, EIS of heteroatom-doped HGFs in SRR. **e**, Arrhenius plot showing linear relationship between logarithmic values of the reciprocal of charge transfer resistance and the reciprocal of absolute temperatures. **f**, Activation energies for the SRR process among various heteroatom-doped HGFs at the onset potential. Error bars in **f** indicate the standard deviation of three independent electrodes.

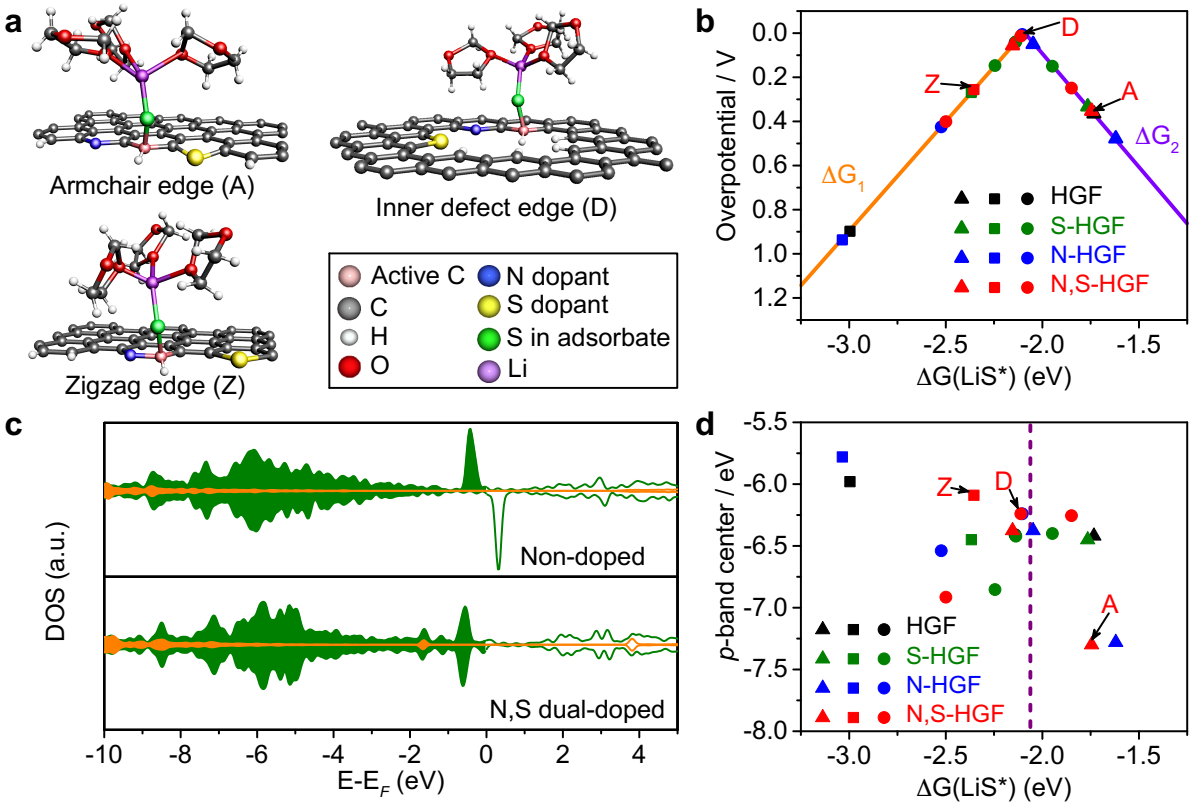

Fig. 4 | Density functional theory calculations on the activity origin of the heteroatom-doped HGFs on SRR. a, Model constructions showing the interaction between three representative active sites in N,S-HGF with the microsolvated sulfur adsorbates. **b**, Volcano plot linking the overpotential for the final step to the adsorption energies of the LiS radical intermediate on different active sites (▲, ■, ● represent the active sites at different armchair edge, zigzag edge and inner defect edge). **c**, *p*-band center shift and modification of the pDOS of the catalytic carbon atoms induced by the N and S dual-doping: non-doped HGF (up) and N,S-HGF (down). **d**, Relation between the *p*-band center and LiS adsorption energy at different active carbon. The purple dashed line represents the adsorption energy associated with the top of the volcano in (**b**). The data points labeled by D, A, Z in (**b**) and (**d**) correspond to the representative structures shown in (**a**).

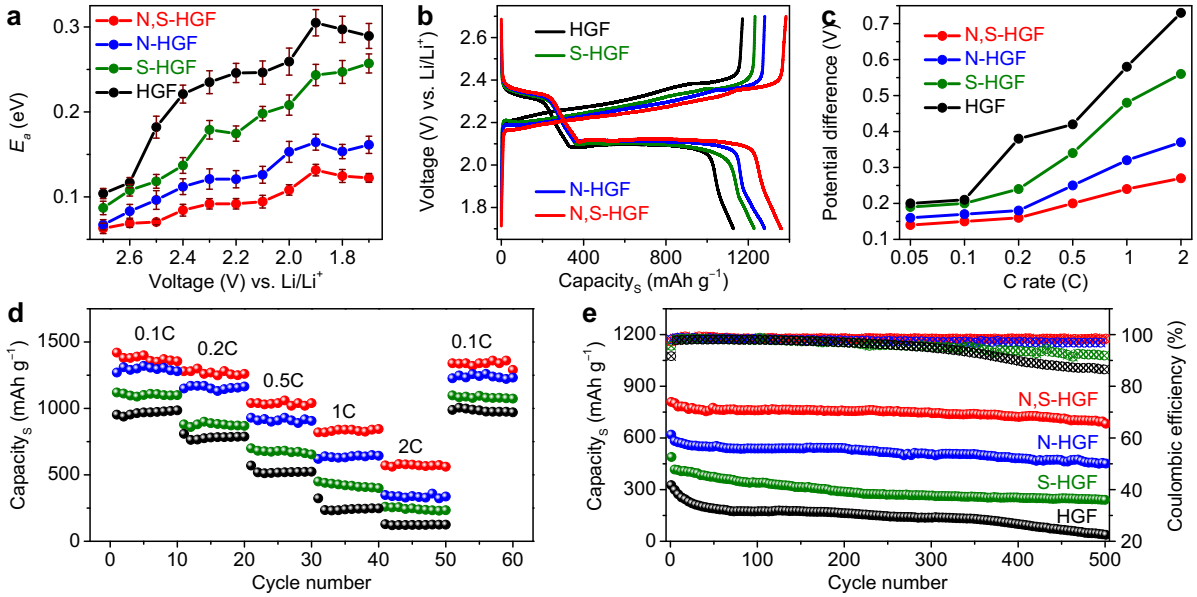

Fig. 5. Activation energy profiles and overall performance of the heteroatom-doped HGF cathodes in Li-S coin cells. a, Activation energies for heteroatom-doped HGFs at various voltages. Error bars in **a** indicate the standard deviation of three independent coin cells. **b**, Charge/Discharge curves of the heteroatom-doped HGFs based sulfur cathodes at 0.1 C. **c**, Potential difference between the anodic and cathodic sweep in heteroatom-doped HGFs at different C rates; **d**, Rate capability of the heteroatom-doped HGFs based sulfur cathodes from 0.1 C to 2 C with the sulfur loading of 4 mg cm^{-2}. **e**, Cycling stability of the heteroatom-doped HGFs based sulfur cathodes at 1 C with the sulfur loading of 4 mg cm^{-2}.